

# A Continuous $hp$ –Mesh Model for Discontinuous Petrov-Galerkin Finite Element Schemes with Optimal Test Functions

Ankit Chakraborty<sup>a</sup>, Georg May<sup>b</sup>

<sup>a</sup>*AICES, RWTH Aachen University, Schinkelstraße 2, 52062 Aachen, Germany*

<sup>b</sup>*Von Karman Institute for Fluid Dynamics, Waterloosesteenweg 72, 1640 Sint-Genesius-Rode, Belgium*

---

## Abstract

We present an anisotropic  $hp$ –mesh adaptation strategy using a continuous mesh model for discontinuous Petrov-Galerkin (DPG) finite element schemes with optimal test functions, extending our previous work [1] on  $h$ –adaptation. The proposed strategy utilizes the inbuilt residual-based error estimator of the DPG discretization to compute both the polynomial distribution and the anisotropy of the mesh elements. In order to predict the optimal order of approximation, we solve local problems on element patches, thus making these computations highly parallelizable. The continuous mesh model is formulated either with respect to the error in the solution, measured in a suitable norm, or with respect to certain admissible target functionals. We demonstrate the performance of the proposed strategy using several numerical examples on triangular grids.

*Keywords:* Discontinuous Petrov-Galerkin, Continuous mesh models,  $hp$ –adaptations, Anisotropy

---

## 1. Introduction

Automatic mesh adaptation algorithms are potent tools that aid the computation of efficient and accurate solutions of partial differential equations (PDEs). These algorithms can significantly increase the accuracy and computational efficiency by modifying the functional space in which the approximate solution is sought.

5 These modifications can be roughly classified into three different categories:

- Modifying the geometrical properties of mesh elements ( $h$ –adaptation);
- modifying the order of approximation space ( $p$ –adaptation);
- combining  $h$ – and  $p$ –adaptation ( $hp$ –adaptation).

In this article, we focus on  $hp$ –adaptation. An automatic  $hp$ –mesh adaptation strategy attempts to produce  
 10 a near-optimal distribution of element size ( $h$ –adaptivity) and combine it with an appropriate distribution of

---

\*Corresponding author

Email address: [chakraborty@ices.rwth-aachen.de](mailto:chakraborty@ices.rwth-aachen.de) (Ankit Chakraborty)

local order of approximation ( $p$ -adaptivity) with the least amount of user's input. Such an automatic mesh adaptation strategy faces the problem of locally choosing between  $h$ -refinement or  $p$ -refinement. This issue has been addressed in the past in many isotropic mesh-adaptation methods [2, 3, 4, 5, 6, 7].

In recent times, metric-based mesh adaptation has emerged as a promising technology for generating meshes, especially for computational fluid dynamics [8, 9, 10]. Meshes comprised of simplices can be represented by a Riemannian metric field. In metric-based mesh adaptation techniques, the parameters defining the metric field are optimized to generate an appropriate mesh. In general, this optimization problem is discrete and defies any analytical solution. However, using the continuous mesh approach [11, 12], one formulates a continuous analog of the discrete mesh optimization problem, thus allowing analytical techniques, such as calculus of variations, to be employed for optimization. Although the mesh generated from the continuous mesh model is not provably optimal, it typically has excellent approximation properties [13, 14, 1, 15, 16]. When these adaptive techniques are combined with higher-order approximation methods, they present themselves as very potent tools for attaining higher accuracy with reduced degrees of freedom [17]. The potency of metric-based adaptation methods stems from the flexibility they provide for the efficient discretization of the computational domain near difficulties such as singularities, interior, and boundary layers. Consult [18, 15, 19, 20] for recent development in the context of metric-based adaptation for hybridized discontinuous Galerkin and discontinuous Galerkin discretizations.

An efficient mesh adaptation algorithm is only a part of the machinery required for computing accurate numerical solutions of PDEs. It complements the numerical method employed to compute the approximate solution. Typically, automatic mesh adaptation algorithms employ some a posteriori measure of error. These measures are computed using the approximate solution. Thus, the accuracy and stability of the underlying numerical scheme become indispensable for accurate mesh adaptations. In terms of robust and stable higher-order methods, discontinuous Petrov-Galerkin schemes (DPG) with optimal test functions have been a critical development over the past decade. Demkowicz and Gopalakrishnan first introduced the DPG methodology with optimal test functions in [21, 22]. The core idea of this approach is to compute a discrete test space such that the best possible discrete inf-sup constant is achieved, thus ensuring higher numerical stability and accuracy. Apart from numerical accuracy and stability, these numerical schemes are accompanied by a residual-based error estimator. Due to the presence of this inbuilt error estimator, the DPG methodology with optimal test functions is tailor-made for mesh optimization [23, 24, 25].

This article proposes a metric-based anisotropic adaptation framework that uses the DPG inbuilt error estimator to generate meshes with optimized size and shape distribution, as well as an optimized polynomial degree distribution, thus complementing the optimal test space with a near-optimal approximation space. The article is structured as follows. First, section 2 briefly discusses PG schemes with optimal test functions. Then, in section 3, we review the relationship between a metric field and a triangular mesh. The proposed method to optimize the local mesh anisotropy and the continuous  $hp$ -mesh model used to determine the

optimal element size and polynomial distribution are discussed in section 4 and section 5, respectively. Finally, in section 6, we provide numerical results, and concluding remarks in section 7.

## 2. Discretization

This section briefly discusses the formulation of DPG schemes with optimal test functions. These schemes can be interpreted as minimum residual methods, which allows derivation of an inbuilt error-estimator in a straightforward way. Let  $\mathbb{X}$  and  $\mathbb{V}$  be Hilbert spaces over  $\mathbb{R}^d$ . We consider a well-posed variational boundary value problem using a continuous bilinear form  $b : \mathbb{X} \times \mathbb{V} \rightarrow \mathbb{R}$ . Here  $\mathbb{X}$  is the approximation space, and  $\mathbb{V}$  is the test space. Let  $\mathbb{X}'$  and  $\mathbb{V}'$  be the respective dual spaces of  $\mathbb{X}$  and  $\mathbb{V}$ . For a given functional  $\ell \in \mathbb{V}'$ , the primal solution can be defined as  $u^* \in \mathbb{X}$  satisfying

$$b(u^*, v) = \ell(v) \quad \forall \quad v \in \mathbb{V}. \quad (1)$$

The bilinear form  $b$  generates a continuous linear operator  $\mathcal{B} : \mathbb{X} \rightarrow \mathbb{V}'$  such that,

$$\langle \mathcal{B}u, v \rangle = \langle u, \mathcal{B}'v \rangle = b(u, v) \quad \forall \quad u \in \mathbb{X}, v \in \mathbb{V}. \quad (2)$$

Thus,  $u^* = \mathcal{B}^{-1}\ell$ . Let  $\mathbb{X}_h \subset \mathbb{X}$  be a finite dimensional subspace of  $\mathbb{X}$ . One can characterize the optimal solution  $u_h^{opt} \in \mathbb{X}_h$  as the one with minimal error in an appropriately chosen norm. Since  $u^*$  is not accessible a priori, it cannot be invoked to define the optimality statement. Instead, the following minimum residual principle can be used

$$u_h^{opt} = \underset{u_h \in \mathbb{X}_h}{\operatorname{argmin}} \|\mathcal{B}u_h - \ell\|_{\mathbb{V}'}^2. \quad (3)$$

On taking the Gateaux derivative of  $\|\mathcal{B}u_h - \ell\|_{\mathbb{V}'}^2$  and using the first order optimality condition, the following variational equation is obtained:

$$\langle \mathcal{B}u_h^{opt}, \mathcal{R}_{\mathbb{V}}^{-1}\mathcal{B}u_h \rangle = \langle \ell, \mathcal{R}_{\mathbb{V}}^{-1}\mathcal{B}u_h \rangle \quad \forall u_h \in \mathbb{X}_h, \quad (4)$$

where  $\mathcal{R}_{\mathbb{V}} : \mathbb{V} \rightarrow \mathbb{V}'$  is the Riesz map. Equation (4) can be redefined as

$$b(u_h^{opt}, v_h) = \ell(v_h) \quad \forall v_h \in \mathcal{R}_{\mathbb{V}}^{-1}\mathcal{B}(\mathbb{X}_h). \quad (5)$$

On defining the energy inner product on  $\mathbb{X}$  as  $a(u, w) = \langle \mathcal{B}u, \mathcal{R}_{\mathbb{V}}^{-1}\mathcal{B}w \rangle$ , we can define a norm on  $\mathbb{X}$  as follows:

$$\|u\|_{\mathbb{X}} = a(u, u) = \|\mathcal{B}u\|_{\mathbb{V}'}^2. \quad (6)$$

Since  $\mathbb{V}$  is infinite-dimensional, the inverse of the Riesz map cannot be computed exactly. In practice, the Riesz map is approximately inverted over an enriched finite dimensional subspace  $\mathbb{V}_r \subset \mathbb{V}$  such that

$M = \dim(\mathbb{V}_r) \geq \dim(\mathbb{X}_h) = N$  [26]. The approximation involves a symmetric Gram matrix which is induced by the inner product on  $\mathbb{V}$ . Thus, a practical implementation of the DPG method aims to find  $u_h \in \mathbb{X}_h$  such that

$$b(u_h, v_h) = \ell(v_h) \quad \forall v_h \in \mathbb{V}_h. \quad (7)$$

where  $\mathbb{V}_h = \text{Range}(F_r)$ , and  $F_r : \mathbb{X}_h \rightarrow \mathbb{V}_r$  represents the approximation of the mapping  $\mathcal{R}_\mathbb{V}^{-1}\mathcal{B}$ .

Let  $\varphi$  be the Riesz representation of the residual, i.e.  $\mathcal{R}_\mathbb{V}\varphi = (\mathcal{B}u_h - \ell)$ . Since it is not possible to compute the exact inverse of  $\mathcal{R}_\mathbb{V}$ , we need to approximate  $\varphi$  using the finite-dimensional subspace  $\mathbb{V}_r$ , i.e.,

$$\langle \mathcal{R}_\mathbb{V}\varphi_h, \psi_i \rangle = (\varphi_h, \psi_i)_\mathbb{V} = \langle \mathcal{B}u_h - \ell, \psi_i \rangle \quad \forall \quad i = 1, \dots, M, \quad (8)$$

where  $\psi_1, \dots, \psi_M$  is any basis for  $\mathbb{V}_r$  and  $\varphi_h$  approximates  $\varphi$ . Let  $\varphi_h = \sum_{j=1}^M \hat{c}_j \psi_j$ . Then from eq. (8), we have

$$\mathbb{G}\mathbf{c} = \mathbf{r},$$

where  $\mathbb{G} \in \mathbb{R}^{M \times M}$  is the Gram matrix with  $\mathbb{G}_{i,j} = (\psi_i, \psi_j)_\mathbb{V}$ ,  $\mathbf{c} = (\hat{c}_1, \dots, \hat{c}_M)^T$ , and  $\mathbf{r} \in \mathbb{R}^M$  with  $r_i = b(u_h, \psi_i) - \ell(\psi_i)$ . Thus, the error in energy norm is approximated by:

$$\|u - u_h\|_\mathbb{X} = \|\ell - \mathcal{B}u_h\|_\mathbb{V}, \approx \|\varphi_h\|_\mathbb{V}. \quad (9)$$

50 The function  $\varphi_h$  is also known as the error-representation function [23, 27]. In this article, we employ the ultra-weak variational formulation for our numerical experiments. Details about the algebraic structure of the corresponding linear system can be found in [26]. The ultra-weak formulation for convection-diffusion and diffusion problems leads to a composite trial space i.e.  $U_h := (u_h, \sigma_h, \hat{u}_h, \hat{\sigma}_h) \in \mathbb{X}_h$ <sup>2</sup> where  $u_h$  approximates  $u$ ,  $\sigma_h$  approximates  $\nabla u$ ,  $\hat{u}_h$  approximates the trace of  $u$  on the mesh skeleton, and  $\hat{\sigma}_h$  approximates the normal  
55 flux on the mesh skeleton with  $u$  being the diffused or the convected quantity. When presenting numerical results in section 6, we refer to the approximate energy norm error  $\|\varphi_h\|_\mathbb{V}$  as  $\|U - U_h\|_E$ .

Next, we briefly discuss the DPG-star method [28]. We employ the DPG-star method to solve a compatible dual problem to obtain an error indicator that can drive goal-oriented adaptations. The DPG-star method has been previously used in this context, both for isotropic  $h$ -adaptation [24] and anisotropic  $h$ -adaptation [1]. Let the strong form of the primal problem be given by

$$Lu = s \quad \text{in } \Omega, \quad Au = g \quad \text{on } \partial\Omega, \quad (10)$$

---

<sup>1</sup>In practice, the basis for  $\mathbb{V}_r$  is enriched by adding higher-order polynomials to the basis of  $\mathbb{X}_h$ . Hence, if the basis functions of  $\mathbb{X}_h$  are obtained using order  $p$  polynomials, then we obtain the basis for  $\mathbb{V}_r$  by employing polynomials of order  $p + \delta p$ .

<sup>2</sup> $\mathbb{X}_h \subset \mathbb{X} = L^2 \times (L^2)^d \times H^{\frac{1}{2}} \times H^{-1}$

where  $\Omega$  is the computational domain,  $L$  is a linear differential operator,  $s \in L^2(\Omega)$ ,  $g \in L^2(\partial\Omega)$ , and  $A$  is a linear differential boundary operator on  $\partial\Omega$ . In this article, we deal with target functionals of the following form:

$$J(u) = \int_{\Omega} j_{\Omega} u \, dx + \int_{\partial\Omega} j_{\partial\Omega} C u \, dx, \quad (11)$$

where  $j_{\Omega} \in L^2(\Omega)$ ,  $j_{\partial\Omega} \in L^2(\partial\Omega)$ , and  $C$  is a boundary operator on  $\partial\Omega$ . We assume that the target functional satisfies the compatibility condition for linear problems [29], i.e.,

$$(Lu, z)_{\Omega} + (Au, C^* z)_{\partial\Omega} = (u, L^* z)_{\Omega} + (Cu, A^* z)_{\partial\Omega}, \quad (12)$$

where  $L^*$ ,  $A^*$  and  $C^*$  are the adjoint operators of  $L$ ,  $A$  and  $C$ . The DPG-star method approximates the solution of the dual problem associated with the target functional in eq. (11). The associated dual problem is given by

$$L^* z = j_{\Omega} \quad \text{in } \Omega, \quad A^* z = j_{\partial\Omega} \quad \text{on } \partial\Omega. \quad (13)$$

An in-depth exposition to the DPG-star method can be found in [28, 24]. The resulting error in the target functional can be bounded as:

$$|J(u - u_h)| \leq \|\mathcal{B}\|^{-1} \|\mathcal{B}u_h - l\|_{V'} \|\mathcal{B}' z_h - J\|_{U'}. \quad (14)$$

In eq. (14),  $\|\mathcal{B}u_h - l\|_{V'}$  is the well-studied energy error estimator for DPG methods whereas for the residual of the dual problem, several error estimators have been proposed [28]. In the present work, we use the DPG-star element error indicator proposed in section 5.2 of [28] for convection-diffusion problems with ultra-weak  
60 formulation:

$$\eta_k^* = \left( \|L^*(v_{h,z}, \boldsymbol{\tau}_{h,z}) - j_{\Omega}\|_{L^2(k)}^2 + \sum_{e \in \partial k \setminus \partial\Omega} h_e \|\llbracket \boldsymbol{\tau}_{h,z} \cdot \mathbf{n} \rrbracket\|_{L^2(e)}^2 + \sum_{e \in \partial k} h_e^{-1} \|\llbracket v_{h,z} \rrbracket\|_{L^2(e)}^2 \right)^{\frac{1}{2}}, \quad (15)$$

where  $v_{h,z}$ ,  $\boldsymbol{\tau}_{h,z}$  represent the approximate adjoint solution,  $\llbracket \boldsymbol{\tau}_{h,z} \cdot \mathbf{n} \rrbracket$  and  $\llbracket v_{h,z} \rrbracket$  represents the jump across the edge  $e$  of length  $h_e$ . We assume that the variational problem is well-posed and  $\mathcal{B}$  is bounded from below. Thus, we can use the product of the energy error estimator and the DPG-star error indicator as a valid error indicator for the goal-oriented mesh adaptations. Since we are using the DPG-star method to solve the dual  
65 problem, we have replaced  $L$  with  $L^*$  in the error estimator from section 5.2 of [28] to obtain eq. (15).

### 3. Mesh representation using metric fields

Next, we provide a short description of mesh representation using Riemannian metric fields. Such metric-based mesh representation provides a convenient way of encoding and manipulating a mesh [11, 12]. In this work,

we concern ourselves with meshes consisting of triangles, but the proposed ideas and formulations can be  
70 extended to tetrahedra [30].

Let  $T_h$  be a given triangulation. Then an element in  $T_h$  can be characterized by a symmetric positive definite matrix. Let  $k \in T_h$  represent an element with  $e_i$ ,  $i = 1, 2, 3$  being the vectorial representation of the edges. Then, there exists a non-degenerate symmetric positive definite matrix

$$\mathbb{M} = \begin{bmatrix} M_{1,1} & M_{1,2} \\ M_{2,1} & M_{2,2} \end{bmatrix} \quad (16)$$

such that each edge is equilateral under the metric induced by  $\mathbb{M}$ , i.e.,

$$e_i^T \mathbb{M} e_i = C \quad \forall \quad i = 1, 2, 3,$$

where  $C > 0$  is a constant. The triangular element can be associated with its circumscribing ellipse, given by  $\{\mathbf{x} \in \mathbb{R}^2 : \mathbf{x}^T \mathbb{M} \mathbf{x} = 1\}$ . This is illustrated in fig. 1.

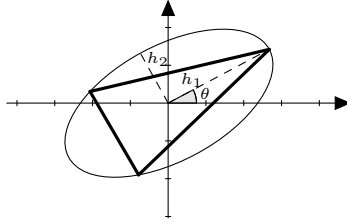


**Figure 1:** Circumscribing ellipse and triangle for  $C = 3$ .

The eigenvectors and the eigenvalues of  $\mathbb{M}$  encode information about the orientation ( $\theta$ ) and the aspect ratio of the ellipse and, subsequently, the associated element. This is evident from the spectral decomposition of  $\mathbb{M}$ :

$$\mathbb{M} = \begin{bmatrix} \cos(\theta) & -\sin(\theta) \\ \sin(\theta) & \cos(\theta) \end{bmatrix}^T \begin{bmatrix} \alpha_1 & 0 \\ 0 & \alpha_2 \end{bmatrix} \begin{bmatrix} \cos(\theta) & -\sin(\theta) \\ \sin(\theta) & \cos(\theta) \end{bmatrix}. \quad (17)$$

The eigenvalues  $\alpha_1 = \frac{1}{h_1^2}$  and  $\alpha_2 = \frac{1}{h_2^2}$  are related to the principal axes of the ellipse. The area of the triangle and the circumscribing ellipse are related by

$$|k| = \frac{3\sqrt{3}}{4} h_1 h_2 = \frac{3\sqrt{3}}{4d}, \quad (18)$$

where  $d$  is called the local mesh density. Note that  $d$  is proportional to inverse of area of the ellipse. The slenderness of the ellipse and the associated triangle is represented by the aspect ratio  $\beta = \frac{h_1}{h_2} \geq 1$ . With  $\theta$ ,  
75  $\beta$ , and  $d$ , one can describe the mesh element geometrically. Typically, most metric-based mesh adaptation algorithms generate a discrete metric field. Metric-based mesh generators suitably interpolate the discrete metric field to produce its continuous equivalent, which is further employed by the mesh generator to produce a metric conforming mesh <sup>3</sup>.

---

<sup>3</sup>A metric conforming mesh contains elements which are nearly equilateral under the input metric field. In this article, we use BAMG[31] as the preferred metric-based mesh generator.

Next, we recall the concept of an  $hp$ -mesh. For a given triangulation  $T_h$ , we associate an integer  $p_k$  with every element  $k \in T_h$ , representing its polynomial order of approximation. These integers form a vector called the polynomial distribution vector:  $\mathbf{p} = (p_k)_{k \in T_h}$ . The triangulation  $T_h$  and the associated polynomial distribution vector  $\mathbf{p}$  form the  $hp$ -mesh  $T_{h,p} := \{T_h, \mathbf{p}\}$ .

#### 4. Anisotropy computation

In this section, we provide a brief description of the methodology employed for computing optimal anisotropy parameters  $(\beta^*, \theta^*)$ . In depth exposition can be found in our previous work [1]. In order to compute the anisotropy parameters  $(\beta^*, \theta^*)$ , we employ the polynomial representation of the error estimator mentioned in eq. (9). In this article, we employ a scaled version of the standard inner product  $(H^1(T_h) \times H(\text{div}, T_h))$  associated with the test space for convection-diffusion and diffusion problems. We call the corresponding test norm as the scaled V-norm [23, 1], given by

$$\begin{aligned} \|(\psi_v, \boldsymbol{\psi}_\tau)\|_{\mathbf{V},k}^2 &= \|\psi_v\|_{2,k}^2 + \sqrt{|k|} \|\nabla \psi_v\|_{2,k}^2 + \|\boldsymbol{\psi}_\tau\|_{2,k}^2 + \sqrt{|k|} \|\nabla \cdot \boldsymbol{\psi}_\tau\|_{2,k}^2 \\ &= \int_k (\psi_v(\mathbf{x}))^2 + \boldsymbol{\psi}_\tau(\mathbf{x}) \cdot \boldsymbol{\psi}_\tau(\mathbf{x}) + \sqrt{|k|} (\nabla \psi_v(\mathbf{x}) \cdot \nabla \psi_v(\mathbf{x}) + (\nabla \cdot \boldsymbol{\psi}_\tau(\mathbf{x}))^2) d\mathbf{x}. \end{aligned} \quad (19)$$

Here  $|k|$  represents the volume of the element  $k \in T_h$  and  $(\psi_v, \boldsymbol{\psi}_\tau)$  are the associated error-representation functions. The computation of optimal anisotropy parameters  $(\beta^*, \theta^*)$  only involves minimization of a bound on the element's energy error estimate (proposed in [1], Section 4). This bound is given by a parameterized integral of  $\beta$  and  $\theta$ . The minimum of the bound is sought iteratively by performing alternate searches in  $\beta$  and  $\theta$  [32].

#### 5. Continuous $hp$ -mesh model

In this section, we present the procedure for  $hp$ -adaptations using the inbuilt error estimator that accompanies DPG schemes with optimal test functions. The procedure is a two-step process that comprises selecting the order of polynomial approximation, which is followed by a mesh density computation. Next, we reiterate an important assumption (see [1, 13]) which is fundamental for the proposed methodology:

**Assumption 5.1:** Let  $T_h$  be a given triangulation and  $\eta_k$  be a local error estimate such that  $\eta^2 = \sum_{k \in T_h} \eta_k^2$  and  $\eta = O(h^s)$  i.e the error estimate converges with order  $s$  [13]. We assume that the local error estimate  $\eta_k$  scales<sup>4</sup> as  $\eta_k = \bar{A}_k |k|^{(s+1)}$ , where  $\bar{A}_k$  depends upon the anisotropy of the element and order of the method  $s$ , but is independent of  $|k|$ . Furthermore, the order of the method  $s$  directly depends upon the polynomial degree of approximation  $p$ .

---

<sup>4</sup>To motivate the scaling  $\eta_k \propto |k|^{(s+1)}$ , recall that the global error estimate  $\eta^2$  scales as  $h^{2s} \propto |K|^s$  (We have a method of order  $s$ ). At the same time, the contribution from each individual sub-element (obtained from local isotropic refinement) scales with an additional factor of  $k$ , because of the local domain of integration. For more details, see section 5, [13]

Verification of assumption 5.1 can be found in [13, 33]. Let  $\{T_h\}_n$  be the sequence of triangulations employed. We intend to construct an error estimate which asymptotically achieves global equality with the inbuilt energy error estimate :

$$\|U - U_h\|_{E,k}^2 \approx e_d(\mathbf{x}_k)|k| \quad \text{for } \mathbf{x}_k \in k, k \in T_h, \quad (20)$$

where we define  $e_d(\mathbf{x}_k)$  as the error density function. Thus asymptotically ( $h \rightarrow 0$ ), we have

$$\|U - U_h\|_{E,\Omega}^2 = \sum_{k \in T_h} e_d(\mathbf{x}_k)|k| \rightarrow \int_{\Omega} e_d(\mathbf{x}) d\mathbf{x}.$$

Using assumption 5.1,  $|k| = \frac{\alpha}{d}$ , and eq. (20), we define the error density function as follows:

$$e_d(\mathbf{x}, p(\mathbf{x})) := \bar{A}(\mathbf{x}, p(\mathbf{x})) d(\mathbf{x})^{-s(\mathbf{x})} \alpha^{s(\mathbf{x})}, \quad (21)$$

where  $\alpha = \frac{3\sqrt{3}}{4}$ . This asymptotic continuous-mesh error model will be used in our  $hp$ -mesh optimization  
 100 scheme below. Using the a priori established order of convergence of the energy estimate [34], we can set  
 $s(\mathbf{x}) = p(\mathbf{x}) + 1$ . In an  $hp$ -adaptive scheme,  $s$  can vary for various elements in the mesh.

### 5.1. Polynomial selection

To choose the order of polynomial approximation for an element, we solve the governing PDE locally over a patch surrounding the element. The boundary conditions for these local problems are obtained using the trace ( $\hat{u}_h$ ) for Dirichlet boundary conditions or the normal flux ( $\hat{\sigma}_h$ ) for Neumann boundary conditions (the traces or the normal fluxes utilized as the local boundary conditions are computed globally for the current polynomial distribution). For complex non-linear problems, choosing local boundary conditions is non-trivial and would need specific analysis. One such example would be the Euler equations, for which one can employ characteristic boundary conditions. In fig. 2, we show an internal patch with Dirichlet boundary condition for a scalar convection-diffusion problem. These local problems are solved at three different polynomial orders,

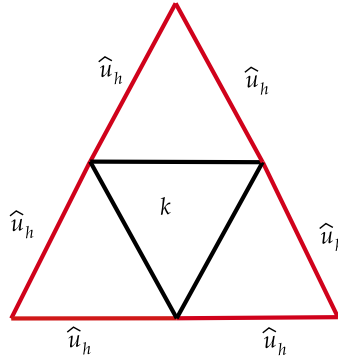


**Figure 2:** Patch around an element  $k$  over which local problems are solved. Edges marked by red represent Dirichlet boundaries of the patch.



$p_k^5$  and  $p_k \pm 1$  where  $p_k$  represents the current polynomial order in element  $k \in T_h$ . Once the solution is computed, it is followed by computing the local energy error estimate  $\|U - U_h\|_{E,k}$  for each polynomial order. Let  $E_{p_k+i}$  and  $N_{p_k+i}$  denote, respectively, the energy error and the number of degrees of freedom, computed at the polynomial order  $p_k + i$ , where  $i = -1, 0, 1$ . Next, we introduce a parameter  $m_{p_k+i}$  which corresponds to the amount of uniform refinement or coarsening required by  $p_k + i$  to achieve the same error as  $p_k$ .

$$m_{p_k+i} = \left( \frac{E_{p_k+i}}{E_{p_k}} \right)^{\frac{2}{s_i+1}} N_{p_k+i}. \quad (22)$$

In eq. (22),  $s_i$  is the a priori rate of convergence for order  $p_k + i$ . For the energy norm, we have used  $s_i = p_k + i + 1$ . In order to choose the optimal polynomial order, we compute  $m_{p_k+i}$  for  $p_k - 1$  and  $p_k + 1$ . The optimal order  $(p_{k,opt})$  is the one which achieves  $E_{p_k}$  with the smallest value of  $m_{p_k+i}$ , i.e.,

$$p_{k,opt} = \underset{i=-1,0,1}{\operatorname{argmin}} m_{p_k+i}. \quad (23)$$

The rationale behind this approach is to find (if possible) a polynomial order, which is more efficient in terms of degrees of freedom required to achieve the same error level as  $p_k$ . For  $i = 0$ , the above computation is trivial.

After we compute the polynomial distribution, we still need to compute the mesh density distribution. For this purpose, we target the continuous error estimate  $E_c = \int_{\Omega} e_d(\mathbf{x}) d\mathbf{x}$  and solve a continuous minimization problem using calculus of variations. This is addressed in the next section. The enrichment  $\delta p$  of the space  $\mathbb{V}_r$  when performing  $hp$ -adaptations is one order higher compared to the enrichment utilized when performing  $h$ -adaptation [1]. This increase in order of enrichment stems from the use of approximation spaces of (up to) order  $p_k + 1$  while solving the local problem.

## 5.2. Mesh density computation

In order to generate the optimal density distribution at fixed cost, we need to define the notion of cost. To that end, we define the mesh complexity  $\mathcal{N}_{h,p}$  as

$$\mathcal{N}_{h,p} = \int_{\Omega} w(p(\mathbf{x})) d\mathbf{x}, \quad (24)$$

where

$$w(p(\mathbf{x})) = \frac{(p(\mathbf{x}) + 1)(p(\mathbf{x}) + 1)}{2}. \quad (25)$$

The relation between the mesh complexity and number of degrees of freedoms ( $N$ ) can be computed as follows:

$$\mathcal{N}_{h,p} = \int_{\Omega} w(\mathbf{x}, p(\mathbf{x})) d\mathbf{x} \approx \sum_{k \in T_h} d(\mathbf{x}_k) w(\mathbf{x}_k, p_k) |k| = \sum_{k \in T_h} \alpha w(\mathbf{x}_k, p_k) = N(Ne, \mathbf{p}). \quad (26)$$

---

<sup>5</sup>To have same fidelity of solution from the local solves at different polynomial orders, we solve the local problem at  $p_k$  rather than using the solution obtained by solving the global system on the current  $hp$ -mesh.

where  $Ne$  is the number of elements and  $\mathbf{p}$  is the polynomial distribution vector associated with the  $hp$ -mesh. Previously, we defined  $\bar{A}(\mathbf{x})$  as a continuous analog of  $\bar{A}_k$  from assumption 5.1. Similarly, we can treat the polynomial distribution vector  $\mathbf{p}$  and introduce a continuous analog  $p(\mathbf{x})$  for the continuous mesh model. The polynomial distribution vector  $\mathbf{p}$  can be seen as a vector created from the snapshots of  $p(\mathbf{x})$  in each element. The continuous analog of  $\mathbf{p}$  and  $\bar{A}_k$  allows us to formulate a continuous optimization problem as follows:

**Problem 5.1:** Let  $\mathcal{N}_{h,p}$  be the desired mesh complexity and  $e_d(\mathbf{x}, p(\mathbf{x}))$  be the error density. We seek a mesh density distribution  $d(\mathbf{x}) : \Omega \rightarrow \mathbb{R}^+$  for a given polynomial distribution  $p(\mathbf{x}) : \Omega \rightarrow Z^+$  such that:

- (a)  $\mathcal{N}_{h,p} = \int_{\Omega} w(\mathbf{x}, p(\mathbf{x})) d(\mathbf{x}) d\mathbf{x}$  with  $w(\mathbf{x}, p(\mathbf{x})) = \frac{2(p(\mathbf{x})+1)(p(\mathbf{x})+2)}{3\sqrt{3}}$ .  
 (b)  $E_c = \int_{\Omega} e_d(\mathbf{x}, p(\mathbf{x})) d\mathbf{x}$  is minimized.

Using eq. (21), the continuous error estimate can be written as

$$E_c = \int_{\Omega} \alpha^{(p(\mathbf{x})+1)} \bar{A}(\mathbf{x}, p(\mathbf{x})) d(\mathbf{x})^{-(p(\mathbf{x})+1)} d\mathbf{x}. \quad (27)$$

In order to compute the minimum, we employ calculus of variations. Taking the variation of the complexity constraint in problem 5.1 with respect to  $d(\mathbf{x})$  yields

$$\delta \mathcal{N}_{h,p} = \int_{\Omega} w(\mathbf{x}, p(\mathbf{x})) \delta d(\mathbf{x}) d\mathbf{x} = 0. \quad (28)$$

Next, on taking the variation of the continuous error estimate with respect to the density, we obtain

$$\delta E_c = \int_{\Omega} -(p(\mathbf{x}) + 1) \alpha^{(p(\mathbf{x})+1)} \bar{A}(\mathbf{x}, p(\mathbf{x})) d^{-(p(\mathbf{x})+2)} \delta d d\mathbf{x}. \quad (29)$$

From eq. (28) and eq. (29), it is implied that

$$\frac{(p(\mathbf{x}) + 1) \bar{A}(\mathbf{x}, p(\mathbf{x}))}{w(\mathbf{x}, p(\mathbf{x}))} \alpha^{(p(\mathbf{x})+1)} d^{-(p(\mathbf{x})+2)} = \text{const}. \quad (30)$$

Solving eq. (30) for  $d(\mathbf{x})$  yields

$$d^*(\mathbf{x}) = \left( \frac{(p(\mathbf{x}) + 1) \bar{A}(\mathbf{x}, p(\mathbf{x})) \alpha^{(p(\mathbf{x})+1)}}{w(\mathbf{x}, p(\mathbf{x}))} \right)^{\frac{1}{(p(\mathbf{x})+2)}} \text{const}^{-\frac{1}{(p(\mathbf{x})+2)}}. \quad (31)$$

Here,  $\text{const}$  does not have a closed form solution. On substituting the expression for optimal density from eq. (31) into the complexity constraint, we obtain

$$\mathcal{N}_{h,p} = \int_{\Omega} w(\mathbf{x}) \left( \frac{(p(\mathbf{x}) + 1) \bar{A}(\mathbf{x}, p(\mathbf{x})) \alpha^{(p(\mathbf{x})+1)}}{w(\mathbf{x}, p(\mathbf{x}))} \right)^{\frac{1}{(p(\mathbf{x})+2)}} \text{const}^{-\frac{1}{(p(\mathbf{x})+2)}} d\mathbf{x}. \quad (32)$$

Equation (32) is non-linear in  $const$  due to the varying exponent. Thus, we need to employ numerical techniques to solve for  $const$ . We use a bisection method to compute this constant in our current work. Once  $const$  is computed, we can substitute its value into eq. (31) to obtain the optimum density distribution  $d^*(\mathbf{x})$ .

The proposed  $hp$ -adaptive algorithm is a generalization of the  $h$ -adaptation [1]. If the variable polynomial distribution is substituted with  $p(\mathbf{x}) = p$  throughout the domain, then  $w(\mathbf{x})$  is constant and the proposed iterative algorithm reverts back to the  $h$ -only adaptation method. Since we are in a discrete setting in terms of triangulation, the quantities  $\bar{A}(\mathbf{x}, p(\mathbf{x}))$ ,  $p(\mathbf{x})$  and optimal density  $d^*(\mathbf{x})$  are computed for each element  $k \in T_h$ . Thus, if  $\mathbf{x}_k \in k$  and  $k \in T_h$ , using assumption 5.1, we have

$$\bar{A}_{k,p_{k,opt}} = \frac{\|U - U_h\|_{E,k,p_{k,opt}}^2}{|k|^{p_{k,opt}+2}} \quad (33)$$

and

$$d^*(\mathbf{x}_k) = \left( \frac{(p_{k,opt} + 1)\bar{A}_{k,p_{k,opt}}\alpha^{(p_{k,opt}+1)}}{w(\mathbf{x}_k, p_{k,opt})} \right)^{\frac{1}{(p_{k,opt}+2)}} const^{-\frac{1}{(p_{k,opt}+2)}}, \quad (34)$$

where  $\|U - U_h\|_{E,k,p_{k,opt}}$  represents the energy error in element  $k$  for the optimal polynomial order  $(p_{k,opt})$  chosen via the process mentioned in section 5.1.

### 5.3. Goal-oriented adaptation

For goal-oriented adaptation, we use the product of the DPG-star error estimate ( $\eta_k^*$ , see eq. (15)) and the energy estimate, i.e.,  $\eta_k = \eta_k^* \|U - U_h\|_{E,k,p_{k,opt}}$  in assumption 5.1 to compute  $\bar{A}_{k,p_{k,opt}}$ . The polynomial order selection process stays the same, as we only depend upon the primal variables and their effect on energy error. For goal-oriented adaptations, we employ  $s(\mathbf{x}) = p(\mathbf{x}) + 1$  in density computations. As previously mentioned in section 5.1 of [1], assumption 5.1 requires sufficient regularity but typically, the regularity of both dual and primal solution can not always be guaranteed. Hence, we pursue a pessimistic approach rather than setting  $s(\mathbf{x}) = 2p(\mathbf{x}) + 1$  for convection-diffusion and diffusion problems.

## 6. Numerical results

### 6.1. Test case I: boundary layer

Sharp boundary layers are one of the most encountered features in fluid dynamics. Through this test case, we present the fidelity of the proposed algorithm in the presence of such boundary layers. In particular, we solve,

$$\begin{aligned} \beta \cdot \nabla u - \epsilon \nabla^2 u &= s & \text{in } \Omega = (0, 1)^2, \\ u &= 0 & \text{on } \partial\Omega, \end{aligned} \quad (35)$$

where  $\beta = [1, 1]^T$  and  $\epsilon > 0$ . The source term  $s(\mathbf{x})$  is chosen in such a manner that the exact solution is given by

$$u(\mathbf{x}) = \left( x + \frac{e^{\frac{x}{\epsilon}} - 1}{1 - e^{\frac{1}{\epsilon}}} \right) \left( y + \frac{e^{\frac{y}{\epsilon}} - 1}{1 - e^{\frac{1}{\epsilon}}} \right), \quad (36)$$

where  $\mathbf{x} = [x, y]^T$ . The strength of the boundary layer is inversely proportional to  $\epsilon$ . The  $hp$ -adaptation is initialized with a mesh comprised of 32 elements and a constant polynomial order of  $p_{initial} = 2$ . Mesh complexity ( $\mathcal{N}_{h,p}$ ) for the first adaptation cycle is computed as

$$\mathcal{N}_{h,p} = Ne \times \frac{(p_{initial} + 1)(p_{initial} + 2)}{2} \times \frac{3\sqrt{3}}{4}, \quad (37)$$

where  $Ne$  represents the number of elements in the mesh. Between each adaptation cycle,  $\mathcal{N}_{h,p}$  is increased by 30%. The choice of growth in  $\mathcal{N}_{h,p}$  is arbitrary. A different choice in growth may result in different pre-asymptotic behavior but should produce a similar asymptotic result.

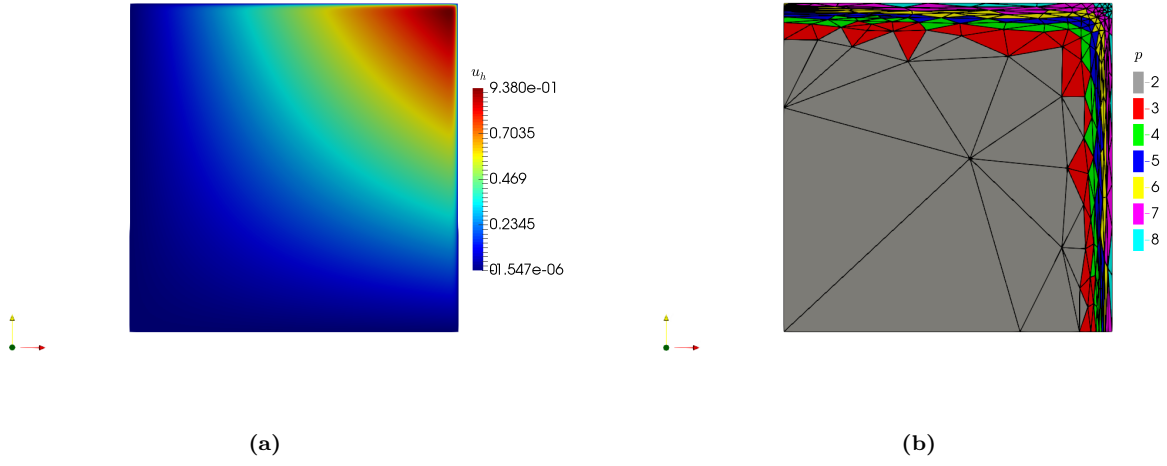


**Figure 3:** Boundary layer: (a) solution contour on an adapted mesh and (b) polynomial distribution on the same adapted mesh with  $\epsilon = 0.005$  and 6980 degrees of freedom.

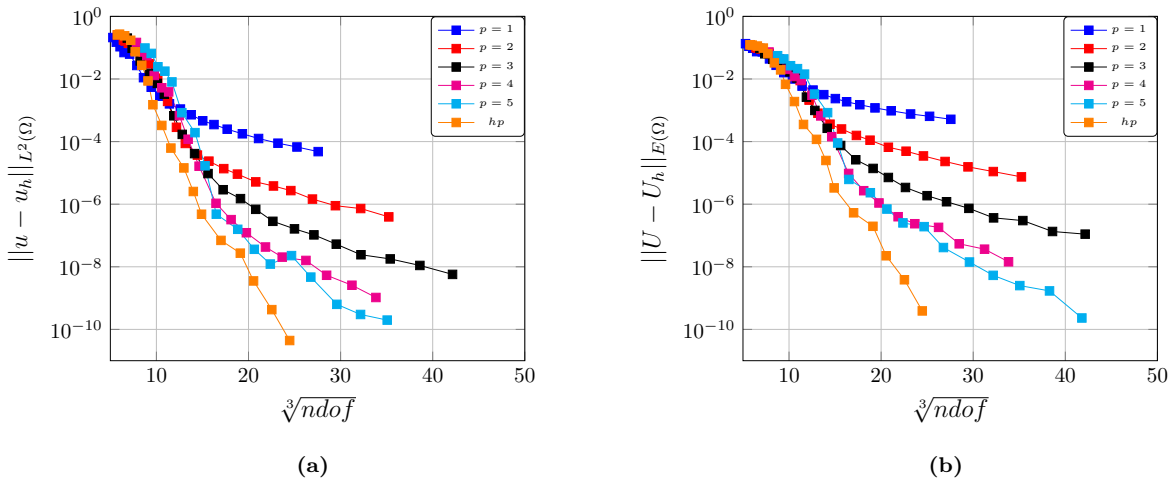


**Figure 4:** Convergence plots of (a)  $L^2$  error in  $u_h$  and (b) energy error using scaled V-norm.

Figure 3 shows a contour plot of the solution obtained on an adapted mesh as well as the corresponding

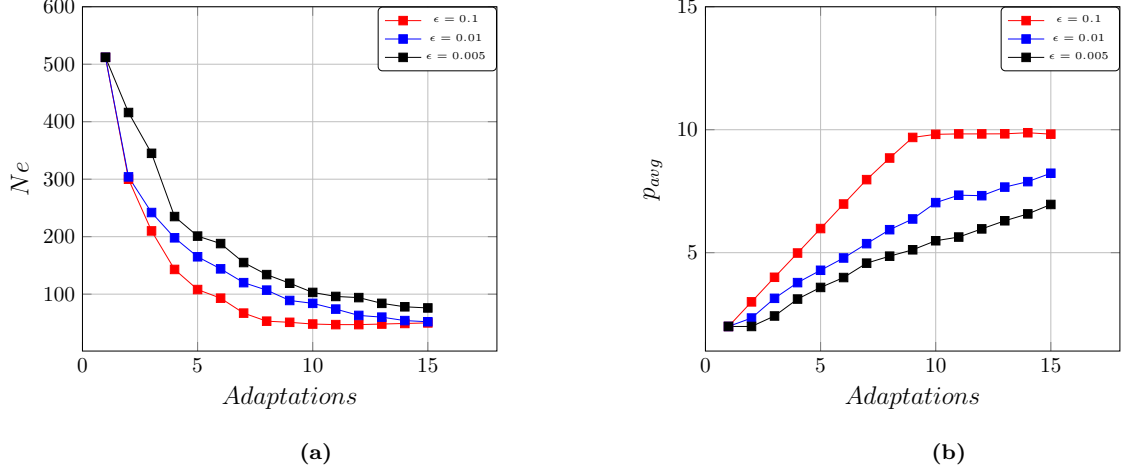


**Figure 5:** Evolution of (a) number of mesh elements and (b) average polynomial order with adaptations using the scaled V-norm at a fixed cost  $\mathcal{N} = 3072$  for different values of  $\epsilon$ .

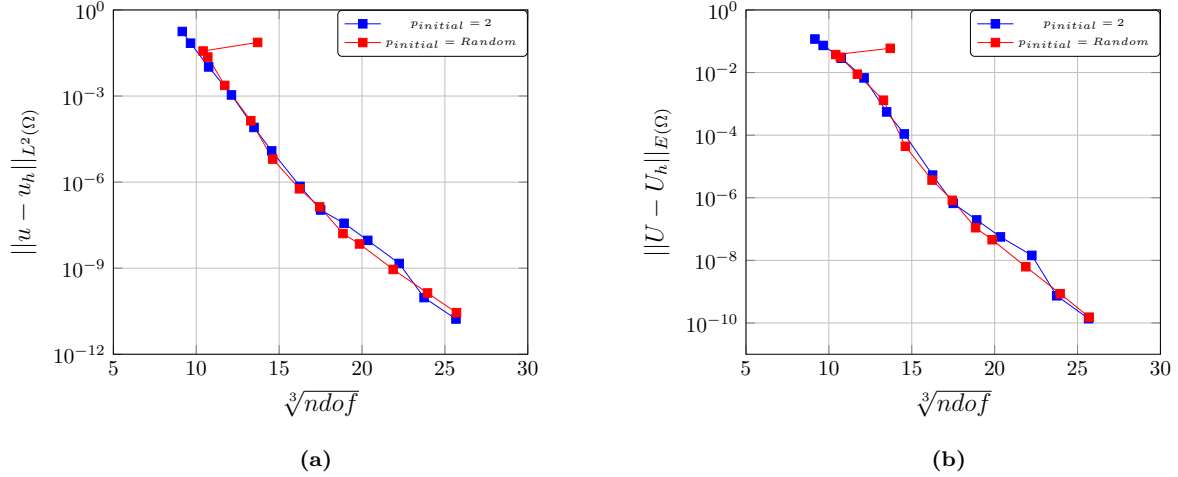


**Figure 6:** Convergence plots of (a)  $L^2$  error in  $u_h$  and (b) energy error using scaled V-norm with different initial polynomial distributions.

polynomial degree distribution. In fig. 4, we present the convergence results comparing the  $h$ -adaptation algorithm [1] and proposed new  $hp$ -adaptation algorithm. On continuously increasing  $\mathcal{N}_{h,p}$ ,  $hp$ -adaptation produces better convergence compared to the  $h$ -adaptation with constant polynomial orders  $p = 1 - 5$ . For all convergence curves, we plot error against  $\sqrt[3]{ndof}$  to verify exponential convergence ( $\|e\|_X \approx Ce^{-bN^{1/3}}$ , [35]). On increasing  $\mathcal{N}_{h,p}$ , initially the adaptation is dominated by  $h$ -refinement. Consequently, once the boundary layer is resolved,  $p$ -refinement starts taking place in the boundary layers along with  $h$ -refinements. The algorithm prefers higher-order polynomials in elements in the boundary layer, whereas it prescribes  $p = 2$  away from the boundary layer. The nature of the analytical solution is approximately quadratic away from the boundary layer, at least up to machine precision, i.e.,  $u(x) \approx xy$  [16]. Since with the assumption of shape-regular elements one can show the equivalence of the scaled V-norm with the  $L^2$  norm of the field

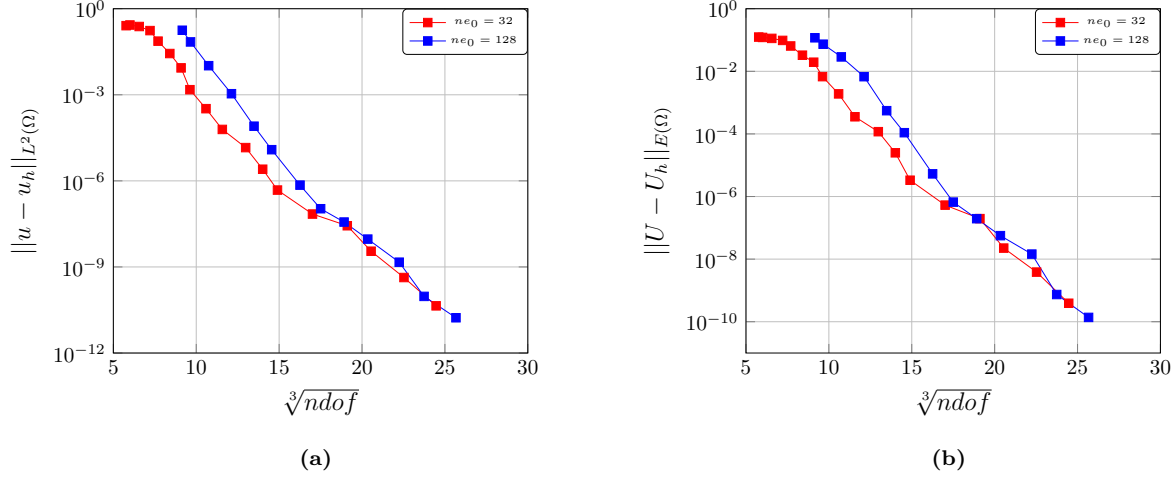


**Figure 7:** Convergence plots of (a)  $L^2$  error in  $u_h$  and (b) energy error using scaled V-norm with different initial mesh.

variables [34], we expect to obtain the polynomial distribution reflecting the local behaviour of the solution variables.

In the next numerical experiment, we perform the adaptation while keeping  $\mathcal{N}_{h,p}$  constant. Here, we have limited  $p_{max}$  (maximum polynomial order in the  $hp$  mesh) at  $p_{max} = 10$ . Since  $u \in C^\infty$ ,  $p_{max}$  will otherwise increase indefinitely. Through this numerical experiment, we intend to observe the interplay between  $h$ - and  $p$ -refinements, which is measured by computing the average polynomial order ( $p_{avg}$ ) in the mesh. The evolution of  $p_{avg}$  with subsequent adaptations is shown in fig. 5 for different values of  $\epsilon$ . For  $\epsilon = 0.005$ ,  $h$ -refinements dominate initial adaptations, and it is only after some initial  $h$ -refinement in the boundary layers that  $p$ -refinements start dominating along with  $h$ -refinements. On increasing  $\epsilon$ , the algorithm performs simultaneous  $p$ -adaptation and  $h$ -adaptation as the boundary layers are smooth enough so as to not require increased spatial resolution for  $p$ -adaptations. This interplay between two adaptive processes is visible from the gradual decrease in the number of elements and subsequent increase in  $p_{avg}$  (see fig. 5).

In many adaptation strategies, the initial conditions such as initial mesh or distribution of the polynomial order may affect the performance. In the proposed  $hp$ -adaptation algorithm, arbitrary coarsening and refinements can be done due to re-meshing. This reduces the dependency of the current mesh on previous iterations. To demonstrate this, we present two instances of variations in initial conditions. First, we use different initial meshes with the same initial polynomial order of approximation (see fig. 7). In second instance, the same initial mesh is used, but one mesh with a random distribution of initial order of approximation (see fig. 6). We observe no deviation in the asymptotic behavior in the convergence plots, showing the proposed methodology's robustness towards these perturbations.

## 6.2. Goal oriented adaptation: Gaussian peak

Next, we present results showing the performance of the proposed  $hp$ -adaptation algorithm for goal-oriented adaptation. The primal problem is the same as that of section 6.1. We consider the solution-dependent (target) functional

$$J(u) = \int_{\Omega} j_{\Omega}(\mathbf{x})u(\mathbf{x}) d\mathbf{x}, \quad (38)$$

where

$$j_{\Omega}(\mathbf{x}) = e^{-\alpha((x-x_c)^2+(y-y_c)^2)}. \quad (39)$$

The target is thus given by a weighted volume integral, where the weight is a Gaussian peak centered at  $(x_c, y_c) = (0.99, 0.5)$ . We choose  $\alpha = 1000$ , leading to a strong localization of the peak (see fig. 8). This leads to the dual problem

$$-\beta \cdot \nabla \bar{\eta} - \epsilon \nabla^2 \bar{\eta} = j_{\Omega} \quad \text{in } \Omega = (0, 1)^2, \quad (40)$$

$$\bar{\eta} = 0 \quad \text{on } \partial\Omega, \quad (41)$$

175 where  $\beta = [1, 1]^T$  and  $\epsilon > 0$ .

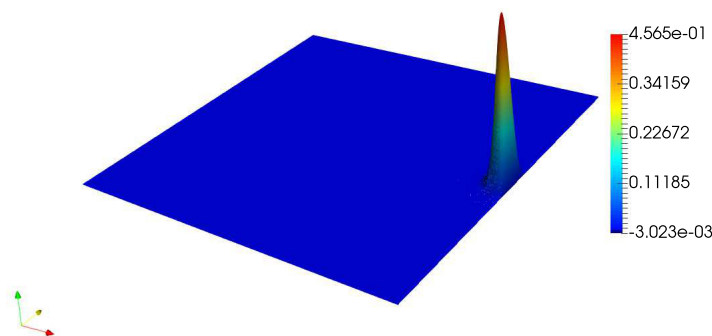


**Figure 8:** Contour showing  $j_{\Omega}(\mathbf{x})$ .

In fig. 9a and fig. 9b, we present the convergence plots comparing  $h$ -adaptation [1] to the proposed  $hp$ -adaptive method. We obtain exponential convergence for  $hp$ -adaptation, thus outperforming  $h$ -adaptation. We present a snapshot of one such mesh in fig. 10. Note that both  $h$ - and  $p$ -refinements mainly take place in the right boundary layer. As we previously observed in section 6.1, the  $h$ -refinements precede  $p$ -refinements, thus following a similar trajectory. The difference here is that only a portion of the boundary layer undergoes  $hp$ -refinement, which the algorithm deems necessary for resolving the target functional. We can notice the saturation of the  $hp$ -convergence curves near machine precision in fig. 9a and fig. 9b.

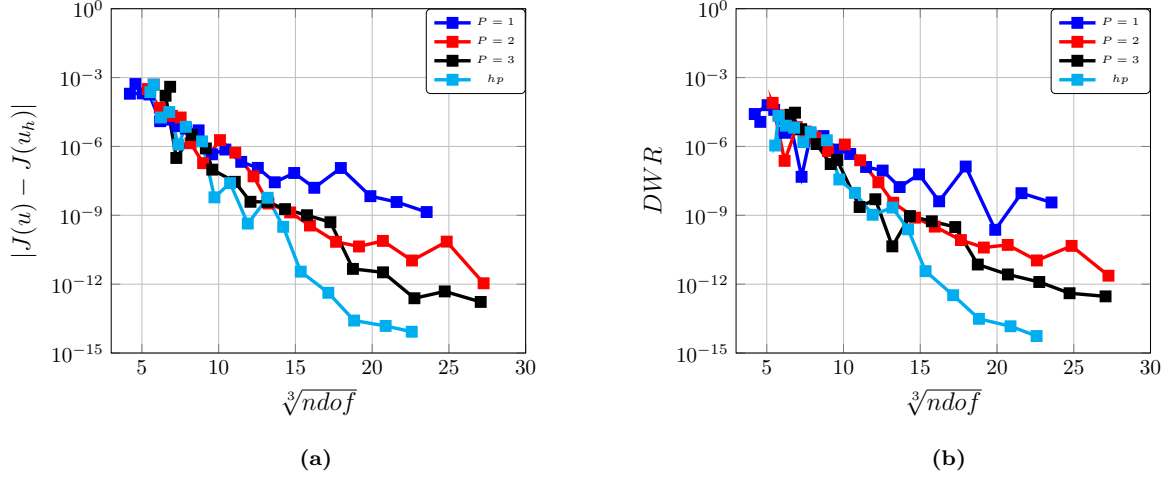


**Figure 9:** Convergence plots for (a) error in target functional and (b) dual weighted residual (DWR) using the scaled V-norm.

Next, we perform a numerical experiment where we keep  $\mathcal{N}_{h,p}$  fixed and then run the adaptations. This numerical experiment aims to examine the algorithm's capacity to distribute the Dofs optimally. It takes only a few adaptations to reach nearly machine precision in terms of the error in target functional.

Adaptation	Ndof	$ J(u) - J(u_h) $	$DWR$
0	3072	1.3599e-04	2.55956e-05
2	2698	2.62413e-09	1.16551e-09
4	3271	1.2955e-11	1.69234e-11
6	3045	2.92165e-12	2.71505e-12
8	3276	3.98067e-14	1.31114e-13

**Table 1:** Adaptation Vs. error for constant complexity using scaled V-norm

$$(\mathcal{N}_{h,p} = \int_{\Omega} w(\mathbf{x}) d(\mathbf{x}) d\mathbf{x} = 3072.0).$$

185

### 6.3. Test case II: inverse tangent - flux target

This numerical experiment compares  $h$ -adaptation [1] and the proposed  $hp$ -adaptation algorithm for a target given by a boundary integral. The governing PDE is the same as in the boundary layer test case (see section 6.1). Here the source term  $s(\mathbf{x})$  is chosen in such a way that the exact solution is given by

$$u(\mathbf{x}) = (\tan^{-1}(\alpha(x - x_1)) + \tan^{-1}(\alpha(x_2 - x))) (\tan^{-1}(\alpha(y - y_1)) + \tan^{-1}(\alpha(y_2 - y))),$$

where  $x_1 = y_1 = \frac{1.0}{3.0}$ ,  $x_2 = y_2 = \frac{2.0}{3.0}$ ,  $\alpha = 50.0$  and  $\epsilon = 0.01$ . The boundary condition is obtained from the exact solution. The target functional is given by:

$$J(u) = \int_{\partial\Omega} j_{\partial\Omega}(\mathbf{x}) \nabla u \cdot \mathbf{n} ds, \quad (42)$$



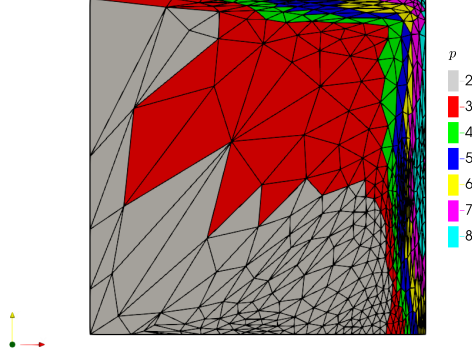


**Figure 10:** Polynomial distribution on an adapted mesh with 11513 degrees of freedom.

where

$$j_{\partial\Omega} = \begin{cases} 1 & \mathbf{n} = (1, 0) \\ 0 & \text{otherwise} \end{cases}. \quad (43)$$

The dual problem has no volumetric source, and the weighting function  $j_{\partial\Omega}(\mathbf{x})$  appears in the boundary condition for the dual problem:

$$-\beta \cdot \nabla \bar{\eta} - \epsilon \nabla^2 \bar{\eta} = 0 \quad \text{in } \Omega = (0, 1)^2, \quad (44)$$

$$\bar{\eta} = j_{\partial\Omega} \quad \text{on } \partial\Omega. \quad (45)$$

In fig. 11, we present the polynomial distribution of an  $hp$ -adapted mesh. Since we are adapting to resolve the flux at  $x = 1.0$  and the convection is in direction  $[1, 1]^T$ , the majority of the  $hp$ -refinement takes place in the right lower diagonal half of the domain (Since the flux on the right boundary depends upon the inlet conditions of the bottom edge at  $y = 0$ , the dual error estimate gives more weighting to the elements in this half.). In fig. 12a and fig. 12b, we present the convergence results. Again we observe exponential convergence in the case of  $hp$ -adaptations.

#### 6.4. Test case III: L-shaped domain

Next, we present the classical L-shaped domain Poisson problem:

$$\begin{aligned} -\nabla^2 u &= s & \text{in } \Omega &= (-1, 1)^2 \setminus [0, 1] \times [-1, 0], \\ u &= g_D & \text{on } \partial\Omega. \end{aligned} \quad (46)$$

The source term  $s(\mathbf{x})$  is chosen in such a way that the exact solution is given by:

$$u(\mathbf{x}) = r^{\frac{2}{3}} \sin\left(\frac{2}{3}\theta\right) \quad \text{where} \quad \theta = \tan^{-1}\left(\frac{y}{x}\right) \quad \text{and} \quad r = \sqrt{x^2 + y^2}. \quad (47)$$

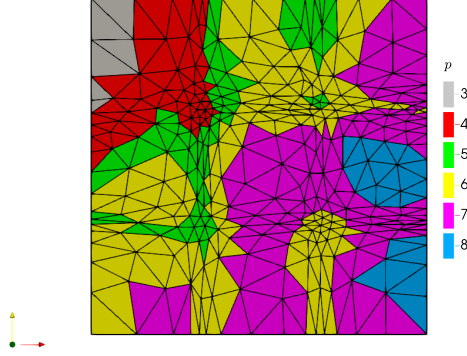


**Figure 11:** Polynomial distribution on an adapted mesh with 15339 degrees of freedom.

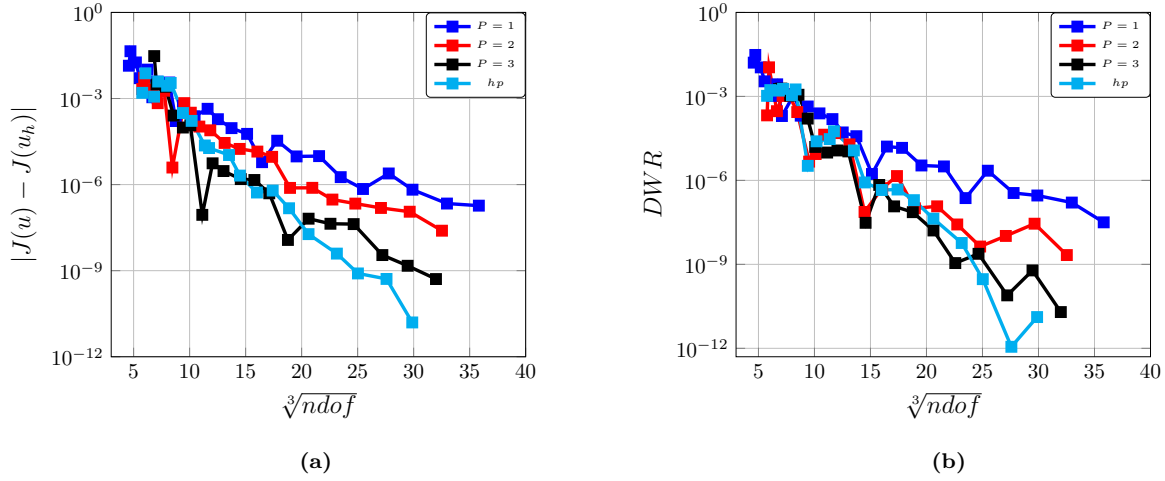


**Figure 12:** Convergence plots for (a) error in target functional and (b) dual weighted residual (DWR) using scaled V-norm.

The boundary conditions are taken from the exact solution. This test case serves to demonstrate the performance of  $hp$ -adaptivity in the presence of a singularity, where the additional flexibility of varying the local order of approximation leads to dramatically improved results compared to  $h$ -only adaptation. In the current example, when using uniform refinement, it is expected to achieve a convergence of  $O(h^{\frac{4}{3}})$  [36] in the  $L^2$  sense in  $u$ . In [37], it has already been shown that higher-order convergence i.e.  $p + 1$  (for  $h$ -adaptation) can be achieved using exponentially graded meshes.

In [35] and [38], it has been shown that exponential convergence can be achieved with a sequence of geometrically refined  $hp$ -meshes in the presence of a corner singularity. However, these meshes are typically hand-crafted and require a priori information (polynomial and size distribution), contrary to an automatic mesh adaptation procedure. Thus, generating such meshes with optimal gradation in size and polynomial distribution is a

challenging problem for any automatic mesh adaptation algorithm.

205 In fig. 13 and fig. 14, we present the convergence results. We observe exponential convergence in  $L^2$  norm, energy norm,  $L^\infty$ ,  $H^1$  norm, and semi-norm. One can observe that  $hp$ -adaptation completely outperforms  $h$ -adaptation.

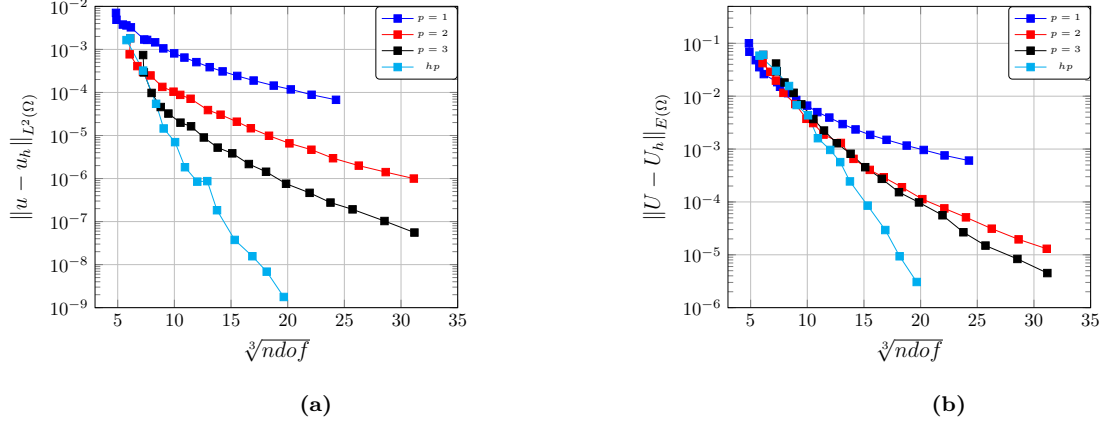


**Figure 13:** Convergence plots of (a)  $L^2$  error in  $u_h$  and (b) energy error using scaled V-norm.

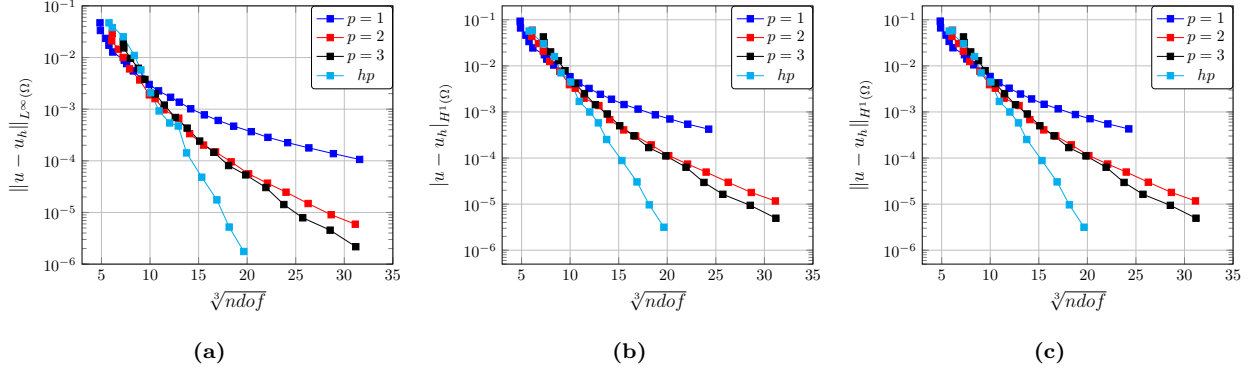


**Figure 14:** Convergence plots of (a)  $L^\infty$  error, (b)  $H^1$  seminorm error and (c)  $H^1$  error using scaled V-norm.

210 In fig. 15, we present the polynomial distribution on an adapted mesh. Near the singularity, we observe the lowest order of approximation. As we move away from the singularity, the algorithm chooses higher polynomial orders due to the smoothness of primal variables.

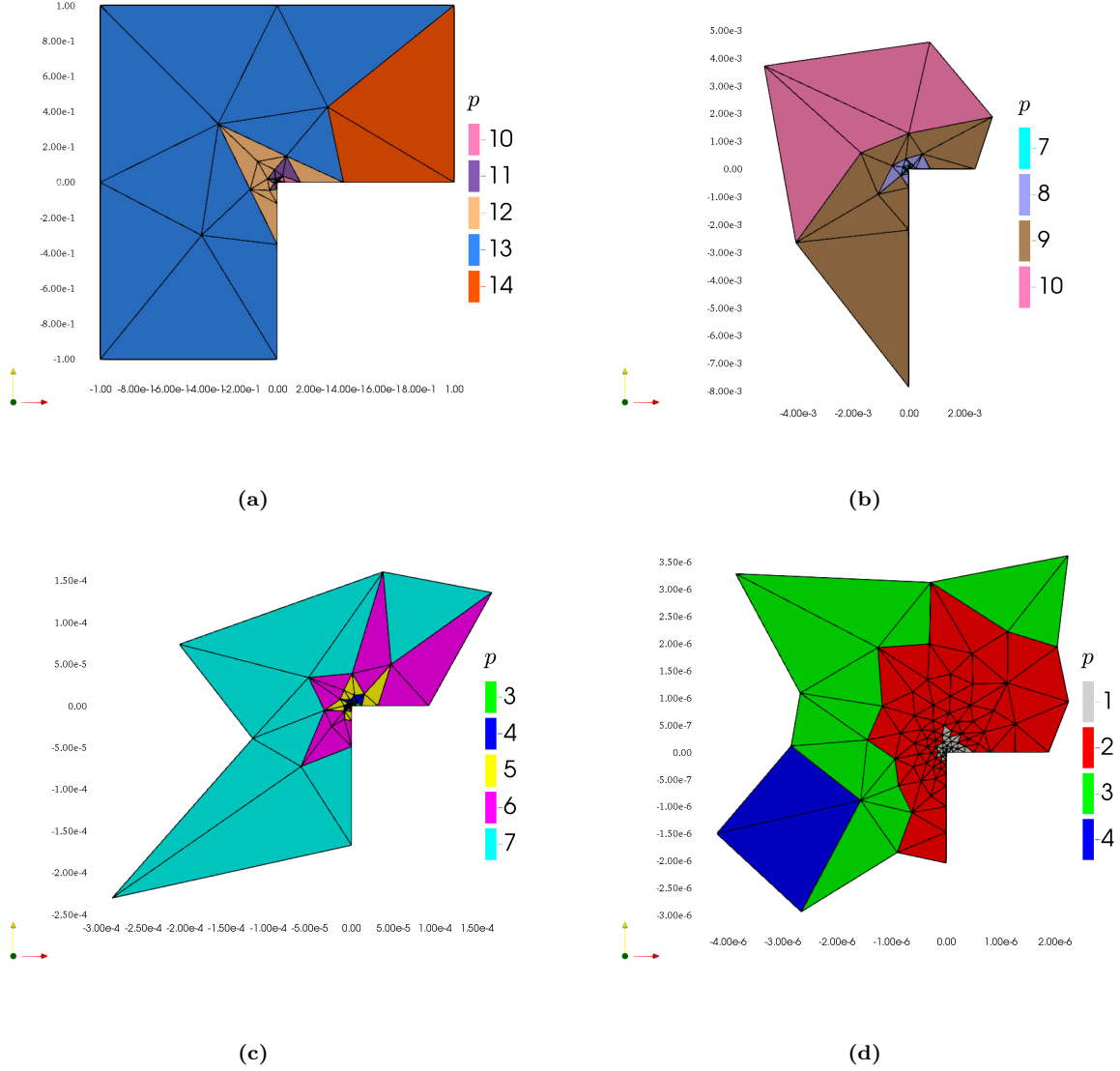


**Figure 15:** Zoomed-in view showing polynomial order with (a) Level 0, (b) Level 1, (c) Level 2 and (d) Level 3 magnification (with Level 0 denoting the least magnification and Level 3 denoting the most magnification).

Finally, we perform a numerical experiment where we keep the required DOFs fixed and adapt the mesh. This numerical experiment aims to demonstrate the reduction in error at a fixed cost. In table 2, it can be observed that there is a reduction in both the  $L^2$  error in  $u$  and the energy error by three orders of magnitude.

## 7. Conclusion and outlook

215 In this article, we present a continuous  $hp$ -mesh model that utilizes the inbuilt residual-based error estimator of DPG finite element schemes with optimal test functions. The model can drive both solution and target-based mesh adaptations. Moreover, the model can be extended to other minimal-residual finite element methods as

Adap no:	0	3	5	7	10
$\ u - u_h\ _{L^2(\Omega)}$	0.000157763	$9.87e - 07$	$1.34e - 07$	$1.13e - 07$	$1.89e - 07$
$\ U - U_h\ _{E(\Omega)}$	0.0251805	$8.05e - 04$	$1.24e - 04$	$3.66e - 05$	$1.98e - 05$
$p_{avg}$	2	2.7	4.01	5.57	6.81
Ndof	3072	2848	3185	3238	3308

**Table 2:** Adaptation vs. error for constant complexity using scaled V-norm ( $\mathcal{N}_{h,p} = \int_{\Omega} w(\mathbf{x})d(\mathbf{x}) d\mathbf{x} = 3072.0$ ).

long as one can localize the error estimate and obtain a polynomial representation of the error estimate. For non-linear problems, the boundary conditions needed for solving the local problems (see section 5.1) on a patch need rigorous analysis. It will depend upon the nature of the non-linear problem and the linearization employed. An extension of the proposed methodology to generate optimal meshes for the compressible Navier-stokes equations is currently being investigated and will be presented in future work.

## 8. Acknowledgment

Funding: This work was funded by the Deutsche Forschungsgemeinschaft (DFG, German Research Foundation) – 333849990/GRK2379 (IRTG Modern Inverse Problems).

Declaration of interest: none

## References

## References

- [1] A. Chakraborty, A. M. Rangarajan, G. May, An anisotropic h-adaptive strategy for discontinuous petrov-galerkin schemes using a continuous mesh model, Computers & Mathematics with Applications 106 (2022) 1–17. doi:<https://doi.org/10.1016/j.camwa.2021.12.001>.
- [2] P. Houston, hp-adaptive discontinuous galerkin finite element methods for first-order hyperbolic problems, SIAM Journal on Scientific Computing 23. doi:[10.1137/S1064827500378799](https://doi.org/10.1137/S1064827500378799).
- [3] S. Giani, P. Houston, Anisotropic hp-adaptive discontinuous galerkin finite element methods for compressible fluid flows., International journal of numerical analysis and modeling. 9 (4) (2012) 928–949.
- [4] P. Houston, hp-adaptive discontinuous galerkin finite element methods for first-order hyperbolic problems, SIAM Journal on Scientific Computing 23. doi:[10.1137/S1064827500378799](https://doi.org/10.1137/S1064827500378799).
- [5] J. Melenk, hp-finite element methods for singular perturbations, Lecture notes in mathematics, v.1796 (2002) 1796. doi:[10.1007/b84212](https://doi.org/10.1007/b84212).

- [6] I. Babuška, M. Suri, The p- and h-p versions of the finite element method, an overview, *Computer Methods in Applied Mechanics and Engineering* 80 (1) (1990) 5–26. doi:[https://doi.org/10.1016/0045-7825\(90\)90011-A](https://doi.org/10.1016/0045-7825(90)90011-A).
- [7] L. Demkowicz, J. Kurtz, D. Pardo, M. Paszynski, W. Rachowicz, A. Zdunek, *Computing with Hp-Adaptive Finite Elements, Vol. 2: Frontiers Three Dimensional Elliptic and Maxwell Problems with Applications*, 1st Edition, Chapman Hall, 2007.
- [8] M. Ceze, K. J. Fidkowski, Anisotropic hp-adaptation framework for functional prediction, *AIAA Journal* 51 (2) (2013) 492–509. doi:10.2514/1.J051845.
- [9] T. Leicht, R. Hartmann, Anisotropic mesh refinement for discontinuous galerkin methods in two-dimensional aerodynamic flow simulations, *International Journal for Numerical Methods in Fluids* 56 (11) (2008) 2111–2138. doi:10.1002/fld.1608.
- [10] T. Leicht, R. Hartmann, Error estimation and anisotropic mesh refinement for 3d laminar aerodynamic flow simulations, *Journal of Computational Physics* 229 (19) (2010) 7344 – 7360. doi:<https://doi.org/10.1016/j.jcp.2010.06.019>.  
URL <http://www.sciencedirect.com/science/article/pii/S0021999110003347>
- [11] A. Loseille, F. Alauzet, Continuous mesh framework part i: Well-posed continuous interpolation error, *SIAM Journal on Numerical Analysis* 49 (1) (2011) 38–60. doi:10.1137/090754078.
- [12] A. Loseille, F. Alauzet, Continuous mesh framework part ii: Validations and applications, *SIAM Journal on Numerical Analysis* 49 (1) (2011) 61–86. doi:10.1137/10078654X.
- [13] V. Dolejsi, G. May, F. Roskovec, P. Solin, Anisotropic hp-mesh optimization technique based on the continuous mesh and error models, *Computers & Mathematics with Applications* 74 (1) (2017) 45–63. doi:10.1016/j.camwa.2016.12.015.
- [14] A. Rangarajan, A. Balan, G. May, Mesh optimization for discontinuous galerkin methods using a continuous mesh model, *AIAA Journal* 56 (10) (2018) 4060–4073. doi:10.2514/1.J056965.
- [15] A. Rangarajan, G. May, V. Dolejsi, Adjoint-based anisotropic hp-adaptation for discontinuous galerkin methods using a continuous mesh model, *Journal of Computational Physics* 409 (2020) 109321. doi:<https://doi.org/10.1016/j.jcp.2020.109321>.
- [16] R. Ajay, Metric based hp-adaptation using a continuous mesh model for higher order schemes (PhD thesis), RWTH Aachen.
- [17] Z. Wang, K. Fidkowski, R. Abgrall, F. Bassi, D. Caraeni, A. Cary, H. Deconinck, R. Hartmann, K. Hillewaert, H. Huynh, N. Kroll, G. May, P.-O. Persson, B. van Leer, M. Visbal, High-order cfd

methods: Current status and perspective, *International Journal for Numerical Methods in Fluids* 72 (2013) 811–845. doi:10.1002/flid.3767.

- [18] N. Ringue, S. Nadarajah, An optimization-based framework for anisotropic hp-adaptation of high-order discretizations, *Journal of Computational Physics* 375 (2018) 589–618. doi:10.1016/j.jcp.2018.09.005.

- [19] V. Dolejší, G. May, A. Rangarajan, A continuous hp-mesh model for adaptive discontinuous Galerkin schemes, *Applied Numerical Mathematics* 124 (September) (2018) 1–21. doi:10.1016/j.apnum.2017.09.015.

URL <https://doi.org/10.1016/j.apnum.2017.09.015>

- [20] J. Dahm, Toward Accurate, Efficient, and Robust Hybridized Discontinuous Galerkin Methods (PhD thesis), The University of Michigan, Ann Arbor.

- [21] L. Demkowicz, J. Gopalakrishnan, A class of discontinuous Petrov-Galerkin methods. Part I: The transport equation, *Computer Methods in Applied Mechanics and Engineering* 199 (23-24) (2010) 1558–1572. doi:10.1016/j.cma.2010.01.003.

- [22] L. Demkowicz, J. Gopalakrishnan, A class of discontinuous petrov-galerkin methods. ii. optimal test functions, *Numerical Methods for Partial Differential Equations* 27 (1) (2011) 70–105. doi:10.1002/num.20640.

- [23] L. Demkowicz, J. Gopalakrishnan, A. Niemi, A class of discontinuous Petrov-Galerkin methods. Part III: Adaptivity, *Applied Numerical Mathematics* 62 (2013) 396–427.

- [24] B. Keith, A. V. Astaneh, L. F. Demkowicz, Goal-oriented adaptive mesh refinement for discontinuous petrov-galerkin methods, *SIAM Journal on Numerical Analysis* 57 (4) (2019) 1649–1676. doi:10.1137/18M1181754.

- [25] The double adaptivity paradigm : (how to circumvent the discrete inf-sup conditions of babuska and brezzi), *Computers & Mathematics with Applications* doi:<https://doi.org/10.1016/j.camwa.2020.10.002>.

- [26] A. Vaziri Astaneh, F. Fuentes, J. Mora, L. Demkowicz, High-order polygonal discontinuous Petrov-Galerkin (PolyDPG) methods using ultraweak formulations, *Computer Methods in Applied Mechanics and Engineering* 332 (July) (2018) 686–711. arXiv:1706.06754, doi:10.1016/j.cma.2017.12.011.

- [27] J. Zitelli, I. Muga, L. Demkowicz, J. Gopalakrishnan, D. Pardo, V. M. Calo, A class of discontinuous Petrov-Galerkin methods. Part IV: The optimal test norm and time-harmonic wave propagation in 1D, *Journal of Computational Physics* 230 (7) (2011) 2406–2432. doi:10.1016/j.jcp.2010.12.001.

- [28] L. Demkowicz, J. Gopalakrishnan, B. Keith, The dpg-star method, *Computers & Mathematics with Applications* 79 (11) (2020) 3092 – 3116. doi:<https://doi.org/10.1016/j.camwa.2020.01.012>.
- 305 [29] R. Hartmann, Adjoint consistency analysis of discontinuous galerkin discretizations, *SIAM J. Numer. Anal.* 45 (2007) 2671–2696. doi:10.1137/060665117.
- [30] A. M. Rangarajan, A. Chakraborty, G. May, V. Dolejsi, A continuous-mesh optimization technique for piecewise polynomial approximation on tetrahedral grids. *arXiv*:<https://arc.aiaa.org/doi/pdf/10.2514/6.2018-3246>, doi:10.2514/6.2018-3246.
- 310 URL <https://arc.aiaa.org/doi/abs/10.2514/6.2018-3246>
- [31] F. Hecht, BAMG: Bidimensional anisotropic mesh generator.  
URL <https://www.ljll.math.upmc.fr/hecht/ftp/bamg>
- [32] V. Dolejší, G. May, A. Rangarajan, F. Roskovec, A Goal-Oriented High-Order Anisotropic Mesh Adaptation Using Discontinuous Galerkin Method for Linear Convection-Diffusion-Reaction Problems,  
315 *SIAM Journal on Scientific Computing* 41 (3) (2019) A1899–A1922.
- [33] D. A. Venditti, D. L. Darmofal, Grid adaptation for functional outputs: Application to two-dimensional inviscid flows, *Journal of Computational Physics* 176 (1) (2002) 40 – 69. doi:<https://doi.org/10.1006/jcph.2001.6967>.
- [34] L. Demkowicz, J. Gopalakrishnan, Analysis of the dpg method for the poisson equation, *SIAM Journal on Numerical Analysis* 49 (2011) 1788–1809.
- 320 [35] B. Guo, I. Babuška, The h-p version of the finite element method, *Computational Mechanics* 1 (3) (1986) 203–220. doi:10.1007/BF00272624.  
URL <https://doi.org/10.1007/BF00272624>
- [36] H. Egger, U. Rude, B. Wohlmuth, Energy-corrected finite element methods for corner singularities, *SIAM Journal on Numerical Analysis* 52 (1) (2014) 171–193. doi:10.1137/120871377.
- 325 [37] M. Yano, An Optimization Framework for Adaptive Higher-Order Discretizations of Partial Differential Equations on Anisotropic Simplex Meshes (PhD thesis), Massachusetts Institute of Technology.
- [38] L. B. da Veiga, A. Chernov, L. Mascotto, A. Russo, Exponential convergence of the hp virtual element method in presence of corner singularities, *Numerische Mathematik* 138 (3) (2018) 581–613. doi:  
330 10.1007/s00211-017-0921-7.  
URL <https://doi.org/10.1007/s00211-017-0921-7>